

# Journal Pre-proof

Radioactive nano-oxygen generator enhance anti-tumor radio-immunotherapy by regulating tumor microenvironment and reducing proliferation

Pei Pei, Wenhao Shen, Yu Zhang, Yanxiang Zhang, Zhongyuan Qi, Hailin Zhou, Teng Liu, Liang Sun, Kai Yang



PII: S0142-9612(21)00682-7

DOI: <https://doi.org/10.1016/j.biomaterials.2021.121326>

Reference: JBMT 121326

To appear in: *Biomaterials*

Received Date: 11 October 2021

Revised Date: 12 December 2021

Accepted Date: 15 December 2021

Please cite this article as: Pei P, Shen W, Zhang Y, Zhang Y, Qi Z, Zhou H, Liu T, Sun L, Yang K, Radioactive nano-oxygen generator enhance anti-tumor radio-immunotherapy by regulating tumor microenvironment and reducing proliferation, *Biomaterials* (2022), doi: <https://doi.org/10.1016/j.biomaterials.2021.121326>.

This is a PDF file of an article that has undergone enhancements after acceptance, such as the addition of a cover page and metadata, and formatting for readability, but it is not yet the definitive version of record. This version will undergo additional copyediting, typesetting and review before it is published in its final form, but we are providing this version to give early visibility of the article. Please note that, during the production process, errors may be discovered which could affect the content, and all legal disclaimers that apply to the journal pertain.

© 2021 Published by Elsevier Ltd.

**Credit Author Statement**

Pei Pei and Wenhao Shen carried out the nanomaterials preparation and immunotherapy experiments

Yu Zhang carried out the cell experiments

Yanxiang Zhang carried out PA imaging experiments

Zhongyuan Qi carried out radiolabeling and SPECT/CT experiments

Hialin Zhou carried out FACS assay

Teng Liu and Liang Sun reviewed the manuscript

Kai Yang provided guidance on experimental design and wrote the manuscript

# **Radioactive Nano-oxygen Generator Enhance Anti-Tumor Radio-immunotherapy by Regulating Tumor Microenvironment and Reducing proliferation**

Pei Pei<sup>#</sup>, Wenhao Shen<sup>#</sup>, Yu Zhang, Yanxiang Zhang, Zhongyuan Qi, Hailin Zhou, Teng Liu, Liang Sun<sup>\*</sup>, Kai Yang<sup>\*</sup>

State Key Laboratory of Radiation Medicine and Protection, School of Radiation Medicine and Protection & School for Radiological and Interdisciplinary Sciences (RAD-X), Collaborative Innovation Center of Radiation Medicine of Jiangsu Higher Education Institutions, Soochow University, Suzhou, Jiangsu 215123, China.

<sup>#</sup>Pei Pei and Wenhao Shen contributed equally to this work.

Corresponding author: kyang@suda.edu.cn, slhmz666@suda.edu.cn.

**Abstract:** Oxygen ( $O_2$ ) is the substance irreplaceable of the body's metabolism, which is not only the primary consumable of life activities, but also provide the input energy for the whole body. Importantly, the  $O_2$  supply will act as an important role in the field of tumor theranostics. Herein, we successfully construct a radioactive nano-oxygen generator ( $^{177}\text{Lu}$ -APPs-PEG) with superior properties, which can not only realize a high-performance radioisotope labelling, but also unfreeze the limitation of  $O_2$  dependence of internal radioisotope therapy (IRT). More importantly, such nano-oxygen generator also can effectively enhance the infiltration of cytotoxic T cells (CTLs) in distant tumors and reduce tumor metastasis. Meanwhile, the increase of  $O_2$  in tumor-site can affect the metabolism of tumor cells and regulatory T (Treg) cells to reduce cancer cells proliferation by down-regulating the expression of hypoxia-inducible factor-1 $\alpha$  (HIF-1 $\alpha$ ) and c-Myc. In short, the strategies we designed provide a new idea for the influence of nano-enzymes on tumor metabolism and immunotherapy.

**Keywords:** Nano-oxygen generator, Radio-immunotherapy, Tumor microenvironment (TME),  $O_2$  supply, Metabolism

## 1. Introduction

Oxygen ( $O_2$ ) is the substance irreplaceable for the body's metabolism, which is not only the primary consumable of life activities, but also provide the input energy for the whole body [1]. Importantly, the degree of oxygen supply determines the health of the body. When the body lacks  $O_2$ , various disease such as anemia, vascular embolism, altitude sickness and other diseases will usually appear [2-6]. Similarly,  $O_2$  also acts as an indispensable role in terms of cancer theranostics [7, 8]. Especially for solid tumors, the rapid growth of tumor cells will generally exceed their blood supply, resulting in the hypoxic microenvironment [9]. Local hypoxia in tumor tissues can increase the level of HIF-1 $\alpha$  and up-regulate vascular endothelial growth factor (VEGF) expression, which will further facilitate the tumor angiogenesis, tumor growth and metastasis [10-13]. Seriously, cancer cells will resistant to radiotherapy and most chemotherapy under such conditions (hypoxic TME) [14-18]. The hypoxic microenvironment can further stimulate tumor cells to produce adenosine molecules, further inducing nearby cytotoxic T cells (CTLs) and natural killer (NK) cells into a dormant state [19, 20]. According to the recent literatures, the increase of  $O_2$  contents in tumor site could promote the degradation of HIF-1 $\alpha$ , further leading to the alterations in the tumor metabolism [21-23].

Therefore, the relieving of cancer hypoxic microenvironment and increasing the  $O_2$  in lesion site may provide a potential method for improving the therapeutic efficiency of tumor. Michail Sitkovsky et al. performed 40~60%  $O_2$  supplement therapy on mice with lung cancer and found that the supplement of  $O_2$  could regulate the TME, allowing more immune cells to enter the tumor-site to produce an anti-tumor immune response, which further inhibit tumor growth [24]. Except directly supplying  $O_2$  to the body, various  $O_2$  carriers (such as hemoglobin and perfluorocarbons) have been designed to efficiently deliver  $O_2$  to tumor-site to relieve the hypoxic microenvironment [25, 26]. Usually, the amount of hydrogen peroxide ( $H_2O_2$ ) in tumor-site tends to be higher than that in normal tissues, which is also one of the reasons for promoting tumor invasion and metastasis [27-30]. However, this feature (high concentration of  $H_2O_2$  in the tumor sites) also provides more strategies for tumor treatment, such as catalysing the decomposition of  $H_2O_2$  in tumor-site to generate  $O_2$  in situ [31-34]. Therefore, catalyze-like  $O_2$  generators such as manganese dioxide ( $MnO_2$ ) and gold-platinum (Au-Pt) nanoparticles have been exploited for endogenous relieving tumor hypoxic microenvironment. Due to the characteristics of low price and high catalytic performance, such  $O_2$  generators have been used in the combination of photodynamic (PDT), photothermal (PTT), chemotherapy, immunotherapy and other therapies, and has produced an excellent synergistic therapeutic effect for cancer [8, 35-39]. In addition, the efficacy of internal radiotherapy will also be affected by the tumor hypoxic microenvironment [40, 41].

In this work, we were committed to prepare a nano-oxygen generator based on the composites of metal-organic framework (MOF) and Au-Pt (APPs), which could not only carry out stable radionuclide labelling, but also efficiently catalyze the decomposition of  $H_2O_2$  at tumor-site to produce  $O_2$ , further unfreezing the limitation of  $O_2$  dependence in internal radioisotope therapy (IRT). More importantly, the increase of local  $O_2$  in distal tumor further heightened the anti-tumor immune response of body after IRT, and meanwhile promoted the infiltration of cytotoxic T cells (CTLs) into the solid tumors. The relieving hypoxic microenvironment in tumor using such  $O_2$  generator would affect the glycometabolism through downregulating HIF-1 $\alpha$  and c-Myc of tumor cells and regulatory T cells (Tregs), further reducing the activity of tumor cells and Tregs, thereby slowing down cancer cell proliferation. Based on the above-mentioned dual effects, the growth of distal tumors was suppressed remarkably after the elimination of primary tumor (**Scheme 1**). In general, the radioactive nano-oxygen generator we developed provided a new way for the combination of radiotherapy and immunotherapy, as well as a new idea for the

## 2. Materials and methods

### 2.1 Materials and Characterization

Meso-Tetra(4-carboxyphenyl) porphine, benzoic acid, zirconium dichloride oxide octahydrate, sodium borohydride ( $\text{NaBH}_4$ ), chloroplatinic acid ( $\text{H}_2\text{PtCl}_6 \cdot 6\text{H}_2\text{O}$ ) and chloroauric acid hydrate ( $\text{HAuCl}_4 \cdot 4\text{H}_2\text{O}$ ) were purchased from Sigma-Aldrich. Antibodies for cell markers and tissue slices were obtained from eBioscience and Abclonal. Radioisotope  $^{177}\text{LuCl}_3$  was purchased from ITG ISotope TechnologI ES Garching GmbH. Characterization of morphology was obtained by a FEI TecnaiG2F20 Field emission transmission electron microscope. The hydrodynamic diameters and zeta potentials were determined by Zetasizer Nano ZS90. Cell analyses were tested by FACSVerse flow cytometer and scanning confocal laser microscope (FV1200, Olympus). The radioactivity was detected by gamma counter (Berthold Technologies GmbH & Co.KG) and radioactivity meter. SPECT/CT images were obtained through a U-SPECT+/CT imaging system (MILABS).

### 2.2 Synthesis of PCN-224 (PCNs)

PCNs was prepared through solvothermal method [42]. In details, 25 mg Meso-Tetra(4-carboxyphenyl) porphine, 700 mg benzoic acid and 75 mg zirconium dichloride oxide octahydrate were evenly dispersed in 30 mL N,N-Dimethylformamide (DMF). Whereafter, the above mixture was stirred and heated to 90 °C for 1 h and then cooled to 25 °C. PCNs were obtained via centrifugation and then washed by DMF for 3 times at 15,000 rpm for 5 min. PCNs was saved in 2 mL DMF for next experiments in the end.

### 2.3 Synthesis of Au-Pt@PCN-224 (APPs)

1 mL PCNs in DMF was firstly mixed with 1 mL methyl alcohol overnight and then washed with deionized water to remove organic solvent for 3 times. Afterwards, PCNs was dispersed in 30 mL water under ice bath condition and 7.5  $\mu\text{L}$   $\text{HAuCl}_4 \cdot 4\text{H}_2\text{O}$  (1 M) and  $\text{H}_2\text{PtCl}_6 \cdot 6\text{H}_2\text{O}$  (1 M) were added to the above solution with stirring, respectively. Thereafter, 1.75 mL  $\text{NaBH}_4$  (1 mg/mL) ice-cold solution was dropwise added into the mixture to in-situ grow Au-Pt nano-enzyme on the surface of PCNs for 1 min. Finally, Au-Pt@PCNs (APPs) were washed with  $\text{H}_2\text{O}$  for 3 times and dispersed in  $\text{H}_2\text{O}$  or DMF. For PEG-modification, 10 mg APPs and 100 mg C18-PMH-terminated PEG (C18-PMH-PEG) were dissolved in 500  $\mu\text{L}$  DMF, which was then dropwise added into 10 mL  $\text{H}_2\text{O}$  under stirring. After 6 h, the PEG modified APPs (APPs-PEG) were dialyzed (MWCO: 8–14 kDa, Dalian Meilune Biotechnology Co, LTD) in  $\text{H}_2\text{O}$  for 24 h to remove DMF. The PEG modification of PCNs was similar to above.

### 2.4 Catalase activity and oxygen production

To verify catalase activity of APPs-PEG, the consumption of  $\text{H}_2\text{O}_2$  was firstly investigated by an indicator, titanium sulfate ( $\text{Ti}(\text{SO}_4)_2$ ), which can occur a chromogenic reaction with  $\text{H}_2\text{O}_2$  [[34]]. Briefly,  $\text{Ti}(\text{SO}_4)_2$  (100 mg) was dissolved into  $\text{H}_2\text{SO}_4$  (16.66 mL) and further diluted by  $\text{H}_2\text{O}$  to 100 mL (solution A). Catalase activity of APPs-PEG was evaluated by mixing APPs-PEG (10  $\mu\text{g}/\text{mL}$ ) with  $\text{H}_2\text{O}_2$  (0.01 M) (solution B). For every 10 min, 2.65 mL of solution A was mixed with 350  $\mu\text{L}$  of solution B to obtain a mixture. The UV-vis absorbance of mixed solution was recorded at 405 nm. To further study the nano-enzyme activity of APPs-PEG, CAT Kit (A007-1-1, Nanjing Jiancheng Bioengineering Institute) was used to detect the CAT relative activity of at different concentration (1.25~10  $\mu\text{g}/\text{mL}$ ). For oxygen production tests, APPs-PEG (10  $\mu\text{g}/\text{mL}$ ) was firstly mixed with  $\text{H}_2\text{O}_2$  (0.01 M) at volume of 10 mL, afterwards, the oxygen content in above mixture was monitored by a portable dissolved oxygen meter.

### 2.5 Radioisotope Labelling and labelling stability assay

For  $^{177}\text{Lu}$  labelling, 2 mCi of  $^{177}\text{Lu}$  ( $^{177}\text{LuCl}_3$ ) in 0.05 M hydrochloric acid solution (5  $\mu\text{L}$ ) was mixed with APPs-PEG or PCNs-PEG (250  $\mu\text{L}$ , 5 mg/mL) in deionized water, respectively, and then sufficiently stirred at 35 °C for 25 min.  $^{177}\text{Lu}$  labelled APPs-PEG ( $^{177}\text{Lu}$ -APPs-PEG) or  $^{177}\text{Lu}$  labelled PCNs-PEG ( $^{177}\text{Lu}$ -PCNs-PEG) were obtained after ultra-filtration purifications for three times. The labelling efficiency were 95.79 % and 94.96 %, respectively. The radiostability method were conducted according to our published work [50].

### 2.6 In vitro experiments

The 4T1 mouse breast cancer cell line (4T1 cells) and human umbilical vein endothelial cell line (HUVEC) were obtained from Cell Source Center, Chinese Academy of Science (Shanghai, China) and cultured under the standard conditions. For biocompatibility evaluation, different concentration of APPs-PEG (0 ~ 200  $\mu\text{g}/\text{mL}$ ) were co-incubated with 4T1 or HUVEC cells for 24 h, and the relative cell viabilities were detected by Cell Counting Kit-8 analysis. For cellular uptake, APPs-PEG

(100 µg/mL) were co-cultured with 4T1 cells for different time (2~12 h) and then harvested for flow cytometry (FACS verse, BD) assay after washing with PBS for 3 times.

For *in vitro* IRT studies,  $^{177}\text{Lu}$ -PCNs-PEG and  $^{177}\text{Lu}$ -APPs-PEG (10 µg/mL) were co-incubated with 4T1 cells at different radioactive dose ( $^{177}\text{Lu}$ : 0, 1.25, 2.5, 5, and 10 µCi) for 24 h under normoxia or hypoxia conditions, respectively. Then, the relative cell viabilities were detected by Cell Counting Kit-8 analysis.

For the clonogenic assay, 4T1 cells were seeded in 6-well plates at densities of 400-1000 cells per well. Afterwards, cells were incubated with  $^{177}\text{Lu}$ -PCNs-PEG and  $^{177}\text{Lu}$ -APPs-PEG (10 µg/mL) with different radioactive dose ( $^{177}\text{Lu}$ : 0, 2.5, 5, 10, and 20 µCi) for 24 h. The surviving fractions were calculated at different time points.

## 2.7 Tumor model

Female BALB/c mice (6~8 weeks) were obtained from Changzhou Cavins Experimental Animal Co. LTD. Animal experiments were performed according to the protocols approved by Soochow University Laboratory Animal Center. 4T1 cells ( $2 \times 10^6$ ) in 50 µL PBS were subcutaneously injected in back of each BALB/c mouse to construct subcutaneous tumor model. All mice were random allocation in experiments. When the volume of tumors exceeded 1,000 mm<sup>3</sup> ( $V_{\text{tumor}} = \text{length} * \text{width}^2/2$ ), mice will be euthanized through carbon dioxide suffocation.

## 2.8 In vivo experiments

4T1 tumor bearing mice were i.v. injected with 200 µL  $^{177}\text{Lu}$ -APPs-PEG (500 µCi, 800 µg/mL corresponding to APPs-PEG) and SPECT/CT images were obtained at different time. For bio-distribution assay, 4T1 tumor-bearing mice were i.v. injected with  $^{177}\text{Lu}$ -APPs-PEG (100 µCi). Mice were then euthanized at 24 h post-injection to obtain the major organs and tumors for gamma counter test.

For subcutaneous tumors treatment, tumor-bearing mice allocated into 5 groups. when tumors volume attained ~85 mm<sup>3</sup>, mice were i.v. injected APPs-PEG (200 µL, 800 µg/mL), Free  $^{177}\text{Lu}$  (200 µL, 300 µCi),  $^{177}\text{Lu}$ -PCNs-PEG (200 µL, 800 µg/mL, 300 µCi),  $^{177}\text{Lu}$ -APPs-PEG (200 µL, 800 µg/mL, 300 µCi) at 0 day, respectively.

For the distant tumors treatment, 4T1 cells were inoculated on two flanks of each mouse back. When tumors volume attained ~85 mm<sup>3</sup>, mice were allocated into 4 groups (G1: Surgery plus PBS (i.v.), G2: Surgery plus APPs-PEG (i.v.), G3:  $^{177}\text{Lu}$ -APPs-PEG (intratumoral injection, (i.t.)) plus PBS (i.v.), G4:  $^{177}\text{Lu}$ -APPs-PEG (i.t.) plus APPs-PEG (i.v.), 5 mice per group). Left flank tumors were surgically removed in G1 and G2 at 0 day. Meanwhile, 25 µL  $^{177}\text{Lu}$ -APPs-PEG (800 µg/mL,  $^{177}\text{Lu}$ : 100 µCi) was i.t. injected in G3 and G4. Mice in G1 and G2 were then i.v. injected with PBS (200 µL per mouse) at 1 and 3 days, however, Mice in G3 and G4 were then i.v. injected with APPs-PEG (200 µL, 800 µg/mL, per mouse) at day 1 and day 3. The growth of the right flank tumors was monitored every 2 day.

## 2.9 Ex vivo analysis of T cells and immunofluorescence slices

For analysing the T cells in distal tumors, cells were stained with anti-CD3-FITC (eBioscience, Clone: 17A2, 11-0032-82), anti-CD8a-PE (eBioscience, Clone: 53-6.7, 12-0081-83) and antiCD4-APC (eBioscience, Clone: GK1.5, 17-0041-83) antibodies to distinguish cytotoxic T lymphocytes (CTLs, CD3<sup>+</sup>CD4<sup>+</sup>CD8<sup>+</sup>) and helper T cells (CD3<sup>+</sup>CD4<sup>+</sup>CD8<sup>-</sup>) by flow cytometer. For the changes in TME, 4T1 tumor-bearing mice were i.v. injected with APPs-PEG (200 µL, 800 µg/mL) at day 1 and day 3. After that, mice were sacrificed and tumors were sliced and stained with Ki67 (A11390, Abclonal), Myc-Tag (AE070, Abclonal), anti- HIF-1α (ab179483, Abcam) and DAPI (ab228549, Abcam) antibody at day 4. Meanwhile, the c-Myc and HIF-1α of regulatory T cells in tumor cells were also analyzed by flow cytometer. In details, cells were firstly stained by following surface antibodies: anti-CD3-FITC (eBioscience, Clone: 17A2, 11-0032-82) and anti-CD4-PerCP. After fixation and permeabilization, cells were stained by anti-FoxP3-PE (eBioscience, Clone: NRRF-30, 72-5775-40), anti-HIF-1α-APC (ThermoFisher, Clone: Mgc3, 17-7528-82) and anti-Myc-Alexa Flour 647 (ab223895, Abcam) and then analysed by flow cytometer.



### 3. Results and discussion

#### 3.1 The fabrication and characterization of radioactive nano-oxygen generator

To construct the radioactive nano-oxygen generator, metal-organic framework PCN-224 (PCNs) were firstly synthesized by solvothermal method [42]. Briefly, Meso-Tetra(4-carboxyphenyl) porphine (TCPP), benzoic acid and zirconium dichloride oxide octahydrate were dissolved by N, N-Dimethylformamide (DMF), which was further heated at 90 °C in oil bath for 1 h. PCNs, which composed of Zr<sub>6</sub> cluster and TCPP, were obtained by further centrifugation and washing. The results of transmission electron microscope (TEM) indicated the successful synthesis of PCNs (**Figure S1&S2**). Afterwards, the Au-Pt nano-enzymes were in-situ grown on PCNs through the NaBH<sub>4</sub> reduction reaction of HAuCl<sub>4</sub>·4H<sub>2</sub>O and H<sub>2</sub>PtCl<sub>6</sub> to obtain nanocomposites Au-Pt@PCN-224 (APPs) (**Figure 1a**). Results displayed that the nano-enzymes were densely decorated on the surface of PCNs (**Figure 1b**). The energy-dispersive X-ray mapping of APPs also revealed the emergence of Au-Pt nano-enzymes on PCNs (**Figure 1c**). Moreover, the growth of nano-enzyme had little effect on the size of PCNs (~ 100 nm) as shown in TEM images (**Figure S1&S2**), which was further confirmed by the dynamic light scattering (DLS) (**Figure 1d**). To further boost the stability of APPs, PEG-grafted poly (maleic anhydride-alt-1-octadecene) (C18-PMH-PEG) was prepared and used for modification of APPs. As shown in **Figure 1d**, the size of PEGylated APPs (APPs-PEG) was 105.7 nm, which was roughly the same as that of PCNs and APPs (**Figure 1b&S2**). In addition, we were surprised to find that the formation of Au-Pt nano-enzymes could transform the zeta potential of PCNs from  $13.9 \pm 0.6083$  mV to  $-5.503 \pm 0.1762$  mV, which could lessen physiological toxicity and increase circulation time of nano-oxygen generator in the body. The Zeta potential of APPs further dropped off to  $-20.93 \pm 0.5508$  mV after PEGylation (**Figure 1e**). It was worth noting that APPs-PEG also demonstrated similar properties to PCNs, such as UV absorption and fluorescence, which facilitated subsequent experiments (**Figure 1f&S3**). Utilizing the TCPP, the porphyrin structure of which is able to form chelating complexes with different types of metal ions, in APPs-PEG and PCNs-PEG, the therapeutic radioisotope <sup>177</sup>Lu could be labelled by chelation, respectively. The results showed that the high radiolabelling yield (95.79 % and 94.96 %) were obtained for APPs-PEG and PCNs-PEG, respectively. The excellent radio-stability (more than 90 %) of <sup>177</sup>Lu labelled APPs-PEG (<sup>177</sup>Lu- APPs-PEG) or PCNs-PEG (<sup>177</sup>Lu- PCNs-PEG) in PBS was observed by gamma counter detection (**Figure 1g**). In general, the morphology and zeta potential of <sup>177</sup>Lu-APPs-PEG after radiolabelling exhibited no obvious change compared with APPs-PEG (**Figure S2&1e**), which was consistent with the stability measurement (**Figure S4**). Therefore, we successfully constructed radioactive nano-oxygen generator.

#### 3.2 Decompose hydrogen peroxide to produce oxygen effectively

After the successful construction of the radioactive nano-oxygen generator, the oxygen production capacity of APPs-PEG was firstly researched through H<sub>2</sub>O<sub>2</sub> consumption test via titanium sulfate (Ti(SO<sub>4</sub>)<sub>2</sub>) as a chromogenic agent at UV-vis absorbance of 405 nm (**Figure S5a**). As shown in **Figure 2a**, the UV spectra of H<sub>2</sub>O<sub>2</sub>-Ti(SO<sub>4</sub>)<sub>2</sub> at 405 nm maintained a linear relation with different concentrations of H<sub>2</sub>O<sub>2</sub> (1.25 mM-40 mM), which could be used to monitor the consumption of H<sub>2</sub>O<sub>2</sub> at different time points. During our experiments, we found that H<sub>2</sub>O<sub>2</sub> (0.01 M) could be continuously and completely decomposed by 10 µg/mL of APPs-PEG in 40 min, which was in sharp contrast with PBS and PCNs-PEG (**Figure 2b**). The above results could be also supported by a fading photograph of H<sub>2</sub>O<sub>2</sub>-Ti(SO<sub>4</sub>)<sub>2</sub> solution (**Figure S5b**). In addition, we investigated the effect of decomposing H<sub>2</sub>O<sub>2</sub> by APPs-PEG nanoparticles at different conditions and found that the catalytic efficiency of nanozymes will decrease to a certain extent when the pH decrease. However, a constant temperature of 37 °C in the body could completely offset the impact of the drop in pH on the nano-oxygen generator (**Figure S6**). Afterwards, in order to explore the persistent catalytic capacity of APPs-PEG, H<sub>2</sub>O<sub>2</sub> were tautologically added in APPs-PEG (10 µg/mL) every 40 minutes. The results showed that such nano-oxygen generator could continuously catalyze the decomposition of H<sub>2</sub>O<sub>2</sub> without affecting their self-activity (**Figure 2c**). At the same time, catalase (CAT)-like activity of APPs-PEG was also evaluated by CAT Kit, indicating that APPs-PEG possessed  $58.58 \pm 1.932$  % CAT relative activity even at the low concentration (1.25 µg/mL) (**Figure 2d**). After ensuring the high-efficiency decomposition ability of APPs-PEG for H<sub>2</sub>O<sub>2</sub>, oxygen production curve of H<sub>2</sub>O<sub>2</sub>-APPs-PEG solutions (APPs-PEG: 10 µg/mL, H<sub>2</sub>O<sub>2</sub>: 0.01 M) was further detected by oxygen meter, which revealed that APPs-PEG could boost oxygen levels from ~8.4 mg/L to ~33.8 mg/L in 5 min (**Figure 2e**). Further evidence of this could be found in a H<sub>2</sub>O<sub>2</sub>-APPs-PEG solution containing a large number of oxygen bubbles (**Figure S5c**). Meanwhile, by repeatedly adding H<sub>2</sub>O<sub>2</sub> to APPs-PEG solution, we found that oxygen could be continuously produced without affecting the catalytic efficiency of nano-oxygen generator, which may be attributed to the inherent properties of nanoenzymes. (**Figure**

2f). Such functionalized nano-oxygen generator owned a remarkable CAT relative activity at very low concentrations, efficient catalysing the decomposition of  $\text{H}_2\text{O}_2$  to produce sufficient  $\text{O}_2$ . All these consequences afforded a solid theoretical foundation for subsequent applications at cellular and animal levels.

### 3.3 Unfreeze the limitation of oxygen dependence of internal radioisotope therapy

Encouraged by the superior properties, we next explored the behaviour of APPs-PEG at the cellular level. As shown in **Figure 3a**, APPs-PEG exhibited a favourable biocompatibility with different cells even 200  $\mu\text{g/mL}$ , and could be effectively swallowed by cancer cells over time (**Figure 3b&c**). Afterwards, the *in vitro* IRT of  $^{177}\text{Lu}$ -APPs-PEG and  $^{177}\text{Lu}$ -PCNs-PEG were evaluated under normoxia condition and hypoxia condition through CCK-8 detection, respectively. As shown in **Figure 3d&e**, under the same radioactive dose (10  $\mu\text{Ci}$ ),  $^{177}\text{Lu}$ -APPs-PEG exhibited greater lethality for tumor cells under both of normoxia condition and hypoxia condition (cell viability of  $37.73\% \pm 1.39\%$  and  $45.46\% \pm 5.26\%$ , respectively) than that of  $^{177}\text{Lu}$ -PCNs-PEG (cell viability of  $47.75\% \pm 2.64\%$  and  $65.97\% \pm 6.72\%$ , respectively), likely owing to the supply of  $\text{O}_2$  by nano-enzyme on APPs. Moreover, we further confirmed the IRT capacity of  $^{177}\text{Lu}$ -APPs-PEG and  $^{177}\text{Lu}$ -PCNs-PEG by clonogenic assay, indicating that the radioactive nano-oxygen generator could bring about more damage for tumor cells compared to  $^{177}\text{Lu}$ -PCNs-PEG (**Figure 3f**).

In view of the high therapeutic efficiency of radioactive nano-oxygen generator at the cellular *in vitro*, we then investigated *in vivo* behaviours of  $^{177}\text{Lu}$ -APPs-PEG. Firstly, the tumor homing ability of  $^{177}\text{Lu}$ -APPs-PEG was evaluated at different time points post administration. In details, mice were intravenously (i.v.) injected 200  $\mu\text{L}$   $^{177}\text{Lu}$ -APPs-PEG (800  $\mu\text{g/mL}$ , 500  $\mu\text{Ci}$ ) and then scanned via U-SPECT+/CT imaging system. As shown in **Figure 4a**, SPECT signals of  $^{177}\text{Lu}$  appeared at lesion-site, indicating passive enrichment capacity of  $^{177}\text{Lu}$ -APPs-PEG for tumor-site compared to free  $^{177}\text{Lu}$  (**Figure S7**), which was further verified by *ex vivo* biodistribution studies (**Figure S8a&b**). Encourage by the above results, the enhanced IRT effect of  $^{177}\text{Lu}$ -APPs-PEG was then evaluated on subcutaneous tumor model under supporting of nano-oxygen generator. Concretely, tumors bearing mice were randomly allotted in five groups (**Figure 4b-f**). (Group 1, Control; Group 2, APPs-PEG (i.v., 200  $\mu\text{L}$ , 800  $\mu\text{g/mL}$ ); Group3, Free  $^{177}\text{Lu}$  (i.v., 200  $\mu\text{L}$ , 300  $\mu\text{Ci}$ ); Group4,  $^{177}\text{Lu}$ -PCNs-PEG (i.v., 200  $\mu\text{L}$ , 800  $\mu\text{g/mL}$ , 300  $\mu\text{Ci}$ ); Group5,  $^{177}\text{Lu}$ -APPs-PEG (i.v., 200  $\mu\text{L}$ , 800  $\mu\text{g/mL}$ , 300  $\mu\text{Ci}$ )). When tumors volume attained  $\sim 85\text{ mm}^3$ , the mice were treated with the related administration. Compared to control and free  $^{177}\text{Lu}$  group, APPs-PEG exhibited a slight tumor growth inhibition effect. Mice treated with  $^{177}\text{Lu}$ -PCNs-PEG showed a certain suppression for tumor growth, prolonging the lifetime of mice to a certain extent. Noticeably, the tumors growth dealt with by  $^{177}\text{Lu}$ -APPs-PEG was prominently suppressed, significantly prolonging the life span of mice by more than 30 days (**Figure 4g&h**). Moreover, during the process of enhanced IRT, the body weights and *in vivo* biological safety evaluation of mice including major organs H&E stained images and blood hematology and biochemistry were also supervised and no noteworthy changes were observed after different treatments (**Figure 4i&S9**).". Additionally, hematoxylin & eosin (H&E) staining and terminal deoxynucleotidyl transferase dUTP nick end labelling (TUNEL) assay were also conducted to valuate morphologic changes and apoptosis of tumor tissue at 3 day post administrations (**Figure 4j&4k**). The most prominent cell death was found in tumor tissue of mice treated with  $^{177}\text{Lu}$ -APPs-PEG. Generally, such oxygen generator we constructed could not only realize a high-performance isotope labelling, but also achieve a high-efficiency IRT. Especially *in vivo* antitumor therapy, by catalysing the decomposition of  $\text{H}_2\text{O}_2$  to generate  $\text{O}_2$  at TME, radioactive nano-oxygen generator effectively unfreezed the limitation of oxygen dependence of IRT, achieving excellent therapeutic effect and prolonging the survival of mice.

### 3.4 Enhance antitumor immune response to distal tumors

The improvement of  $\text{O}_2$  content in tumor-site has been proved to be one of the important means to intensify the therapeutic effect of cancer including chemotherapy, radiotherapy. Recently, with the booming of tumor immunotherapy,  $\text{O}_2$  has also been found to regulate the TME and allow immune cells to enter the tumor for enhancing an anti-tumor immune response. It had been proved that radioactive nano-oxygen generator could effectively catalyze  $\text{H}_2\text{O}_2$  to produce  $\text{O}_2$ , and possessed a good anti-tumor reaction. In order to further verify whether it could enhance the anti-tumor immune response, distal tumor model was firstly constructed to investigate therapeutic effect of APPs-PEG (i.v.) after elimination of the *in situ* tumors by enhanced IRT of  $^{177}\text{Lu}$ -APPs-PEG (i.t.) or surgery (**Figure 5a**). Meanwhile, tumor retention ability of  $^{177}\text{Lu}$ -APPs-PEG was explored after intra-tumor injection. As shown in SPECT/CT images (**Figure 5b**) and *ex vivo* biodistribution studies (**Figure S8c**),  $^{177}\text{Lu}$ -APPs-PEG revealed a long-term retention at tumor-site even at 24 h post administration, which was beneficial for



subsequently enhanced *in vivo* IRT. In distant tumor model, when tumors volume attained  $\sim 85 \text{ mm}^3$ , mice were randomly allotted in 4 groups randomly ( $n = 5$  per group) (Group 1, surgery (0 day) plus PBS (i.v., 200  $\mu\text{L}$ , 1, 3 day); Group 2, surgery (0 day) plus APPs-PEG (i.v. 200  $\mu\text{L}$ , 800  $\mu\text{g/mL}$ , 1, 3 day); Group 3,  $^{177}\text{Lu}$ -APPs-PEG (i.t., 25  $\mu\text{L}$ , 800  $\mu\text{g/mL}$ , 100  $\mu\text{Ci}$ ) plus PBS (i.v., 200  $\mu\text{L}$ , 1, 3 day); Group 4,  $^{177}\text{Lu}$ -APPs-PEG (i.t., 25  $\mu\text{L}$ , 800  $\mu\text{g/mL}$ , 100  $\mu\text{Ci}$ ) plus APPs-PEG (i.v. 200  $\mu\text{L}$ , 800  $\mu\text{g/mL}$ , 1, 3 day). After that, the volume of distant tumors were measured. In **Figure. 5c**, the growth of distant tumors in group 2 and group 3 showed a slight inhibition compared with group 1, which might be due to a relieved TME or activation of an anti-tumor immune response. However, it was worth noting that the mice in which  $^{177}\text{Lu}$ -APPs-PEG eliminated tumors in situ and further assisted by APPs-PEG showed a great inhibition on distant tumors and survival time of four-fifths mice was more than 30 days (**Figure 5d**). In the meantime, the body weights were also supervised in the course of various treatments and no noteworthy changes were observed post treatments, revealing that our therapeutic strategies have no prominent negative side effects on mice (**Figure S10**). Under the premise of such preeminent therapeutic effect, the anti-tumor immune mechanisms combining enhanced IRT and APPs-PEG were further explored subsequently. Firstly, to obtain the immune cells at day 7 post IRT, cell suspension was acquired from distant tumors and stained by corresponding antibodies to assess the ratio of CD8 + cytotoxic T lymphocytes (CTLs) via flow cytometry assay. Astonishingly, compared to other groups, it was discovered that the ratio of CTLs exhibited a distinct increase, which was up-regulated to  $51.93 \pm 2.25\%$  after combining IRT and nano-oxygen generator (**Figure 5e&f**). This result showed that the improvement of the TME, especially the alleviation of hypoxia, is conducive to the infiltration of immune cells to the tumor-site. In addition, at 25 days after the first treatment, some of the mice from different groups were euthanized to obtain lung tissues for H&E staining. Importantly, the number of metastatic lesions were significantly inhibited by radioactive nano-oxygen generator combined with APPs-PEG (**Figure 5g**). Overall, our experimental results exhibited that the radio-immunotherapy from  $^{177}\text{Lu}$ -APPs-PEG plus APPs-PEG not only could effectively eliminate in situ tumors, but also enhance the infiltration of CTLs into solid tumors and reduce the tumor metastasis by regulating the TME through  $\text{O}_2$  supply.

### 3.5 Affect the glycometabolism and slow down the proliferation of tumors

In addition to directly enhancing the infiltration of CTLs into solid tumors, the increase in  $\text{O}_2$  levels in TME has also been proved to regulate tumor metabolism, thereby affecting anti-tumor immune response [43]. As we all known, normally differentiated cells mainly rely on the oxidative phosphorylation of mitochondria to obtain cell energy, while most tumor cells rely on aerobic glycolysis [44]. HIF-1 $\alpha$  and c-Myc play crucial roles in regulating glycolysis, therefore, the downregulation of which resulting in diminished pyruvate to lactate flux can effectively inhibit the glycolysis of cells in tumor site [45-47]. Treg cells are a major obstacle to tumour immunity. Whereas, *in vivo* HIF-1 $\alpha$ -deficient Treg cells revealed impaired suppressive function, which provides theoretical foundation for reducing the expression of HIF-1 $\alpha$  as a method of targeting Treg cells [48]. However, the improvement of  $\text{O}_2$  in TME is the key factor to downregulate the expression of HIF-1 $\alpha$  and c-Myc. Therefore, in our designed work, nano-oxygen generator in distant tumor model may produce a deeper effect. To investigate the role and mechanism of nano-oxygen generator, photoacoustic (PA) imaging was firstly carried out to observe the  $\text{O}_2$  content in TME by monitoring oxyhemoglobin ( $\text{HbO}_2$ ) in real time (**Figure 6a**). By PA imaging, tumor deoxyhemoglobin (Hb) and  $\text{HbO}_2$  were detected by excitation wavelengths at 750 and 850 nm separately. As shown in **Figure 6b&c**,  $\text{HbO}_2$  (red) signal was prominently increased post i.v. injected with APPs-PEG, indicating the improvement of  $\text{O}_2$  in TME by nano-oxygen generator. A similar result could also be found in hypoxia slices (**Figure S11**). Moreover, we have further evaluated the regulation period of TME by nano-oxygen generator through pimonidazole staining at different time points, indicating that oxygen generator could continuously relieve the hypoxic microenvironment of tumor (**Figure S12**). Afterwards, the tumors were further collected for immunofluorescence staining analysis by laser scanning confocal microscopy (**Figure 6d, e&g**). Notably, it was discovered that the expression of HIF-1 $\alpha$  and c-Myc exhibited prominently decrease after APPs-PEG post injection, which might be attributed to the produce of  $\text{O}_2$  in tumor site. Surprisingly, the proliferation activity of tumor cells was obviously reduced through Ki67 staining in comparison with the control group (**Figure 6f&g**), further proofing that the downregulation of HIF-1 $\alpha$  and c-Myc by nano-oxygen generator could reduce the glycolysis of tumor cells and slow down cell proliferation. In addition, with the changes in TME and metabolism, the proportion of CD3+CD4+FoxP3+ regulatory T (Treg) cells was also found to down-regulate to a certain extent from  $33.75 \pm 3.91\%$  to  $19.02 \pm 6.15\%$  through flow cytometry assay (**Figure 6h&i**). Subsequently, the expression of HIF-1 $\alpha$  and c-Myc in Treg cells were also confirmed via flow cytometry assay. In **Figure 6j&k**, the fluorescence value of HIF-1 $\alpha$  and c-Myc in

Treg cells notably decreased in comparison with the control group, which further proved such nano-oxygen generator mediated metabolic changes of TME could not only reduce the proliferation of tumor cells, but also down-regulate the proportion of Treg cells in TME and further enhanced the efficacy of CTLs. In general, in our study, we found that APPs-PEG could improve the anti-tumor immune response after enhanced IRT through two pathways, including directly improving O<sub>2</sub> content to enhance the infiltration of CTLs and reducing the metabolism of tumor cells and Treg cells to reduce their proliferation (**Figure 6I**).

#### 4. Conclusion

In summary, we had successfully constructed the radioactive nano-oxygen generator with excellent properties. Utilizing such intrinsic properties, high-performance <sup>177</sup>Lu labelling was performed. The remarkable CAT relative activity of APPs-PEG at very low concentrations could significantly catalyze the decomposition of H<sub>2</sub>O<sub>2</sub>, producing sufficient O<sub>2</sub> in the tumor sites. Given the O<sub>2</sub> supplying in TME, such radioactive nano-oxygen generator effectively unfreezed the limitation of O<sub>2</sub> dependence of IRT, realizing an excellent therapeutic effect and prolonging the survival of mice. Remarkably, in the distant tumor model, we found that radio-immunotherapy by <sup>177</sup>Lu-APPs-PEG plus APPs-PEG not only could effectively eliminate in situ tumors, but also enhanced the infiltration of CTLs into solid tumors and reduced the tumor metastasis by regulating the TME via O<sub>2</sub>. Through the analysis of the TME, we further found the mechanism of the anti-tumor immune effect of APPs-PEG after enhanced IRT, including directly improving O<sub>2</sub> content to enhance the infiltration of CTLs and reducing the metabolism of tumor cells and Treg cells to reduce tumor cell proliferation. Therefore, the radioactive nano-oxygen generator we developed provided a new way for the combination of radiotherapy and immunotherapy, as well as a new idea for the influence of nano-enzymes on tumor metabolism and immunotherapy in the future.

#### Acknowledgements

This work was partially supported by the National Natural Science Foundation of China (31822022, U1932208, 32171382, 32000990), the Natural Science Foundation of Jiangsu Province (BK20180094, BK20190946), the Project Funded by the Priority Academic Program Development of Jiangsu Higher Education Institutions (PAPD).

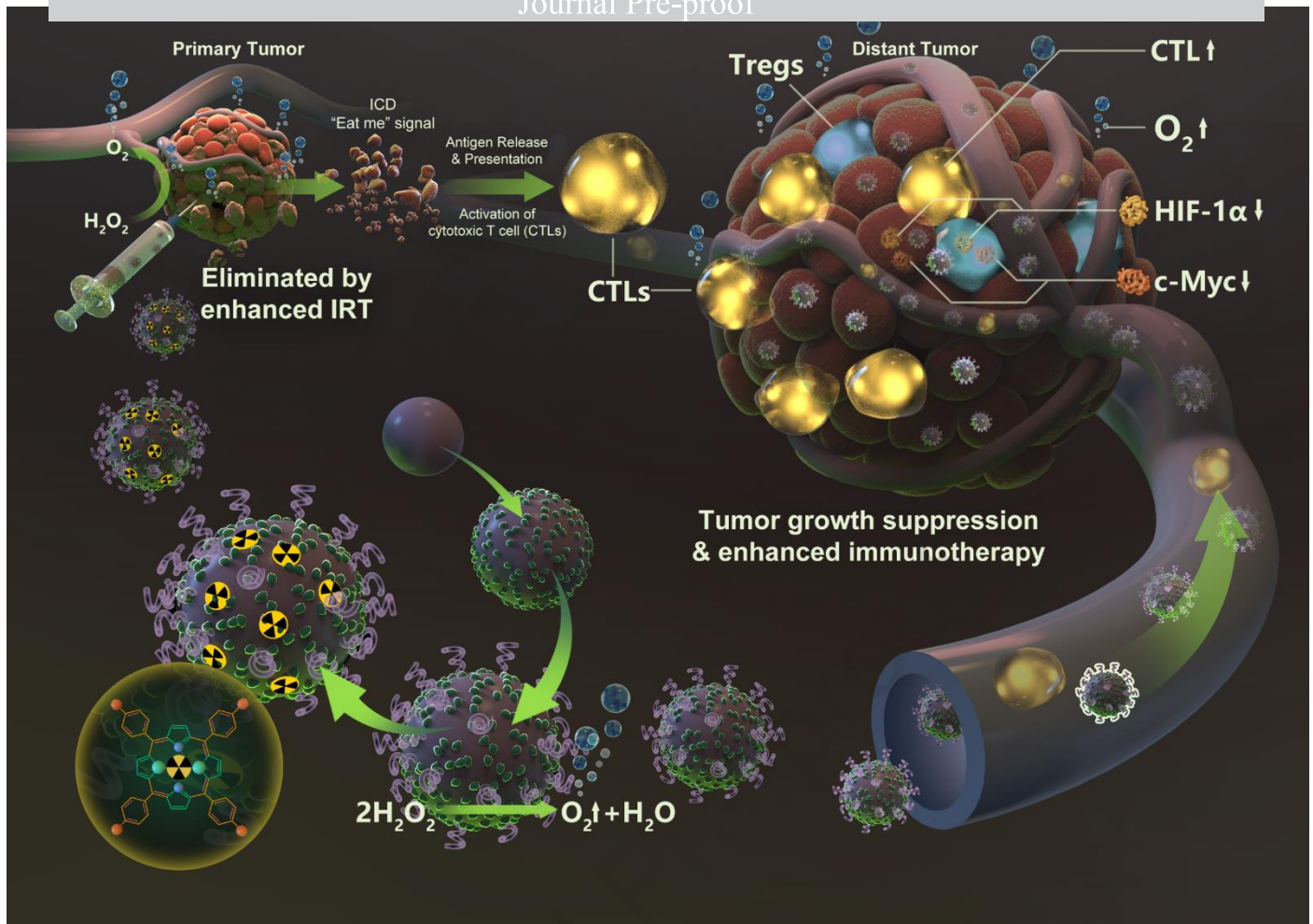
## References

- [1] G.L. Semenza, Life with oxygen, *Science* 318(5847) (2007) 62-64.
- [2] C.E. Cross, B. Halliwell, E.T. Borish, W.A. Pryor, B.N. Ames, R.L. Saul, J.M. McCord, D. Harman, Oxygen Radicals and Human-Disease, *Ann Intern Med* 107(4) (1987) 526-545.
- [3] K. Datta, S. Sinha, P. Chattopadhyay, Reactive oxygen species in health and disease, *Natl Med J India* 13(6) (2000) 304-310.
- [4] A.L. Gill, C.N. Bell, Hyperbaric oxygen: its uses, mechanisms of action and outcomes, *QJM* 97(7) (2004) 385-95.
- [5] B. Halliwell, J.M.C. Gutteridge, Oxygen-Toxicity, Oxygen Radicals, Transition-Metals and Disease, *Biochem J* 219(1) (1984) 1-14.
- [6] G.L. Semenza, Oxygen Sensing, Homeostasis, and Disease REPLY, *New Engl J Med* 365(19) (2011) 1846-1846.
- [7] F. Gao, J. Wu, H. Gao, X. Hu, L. Liu, A.C. Midgley, Q. Liu, Z. Sun, Y. Liu, D. Ding, Y. Wang, D. Kong, X. Huang, Hypoxia-tropic nanozymes as oxygen generators for tumor-favoring theranostics, *Biomaterials* 230 (2020) 119635.
- [8] M. Wang, M. Chang, Q. Chen, D. Wang, C. Li, Z. Hou, J. Lin, D. Jin, B. Xing, Au2Pt-PEG-Ce6 nanoformulation with dual nanozyme activities for synergistic chemodynamic therapy / phototherapy, *Biomaterials* 252 (2020) 120093.
- [9] D.C. Singleton, A. Macann, W.R. Wilson, Therapeutic targeting of the hypoxic tumour microenvironment, *Nat Rev Clin Oncol* 18(12) (2021) 751-772.
- [10] P. Chen, X. Duan, X. Li, J. Li, Q. Ba, H. Wang, HIPK2 suppresses tumor growth and progression of hepatocellular carcinoma through promoting the degradation of HIF-1 $\alpha$ , *Oncogene* 39(14) (2020) 2863-2876.
- [11] C.R. Jung, K.S. Hwang, J. Yoo, W.K. Cho, J.M. Kim, W.H. Kim, D.S. Im, E2-EPF UCP targets pVHL for degradation and associates with tumor growth and metastasis, *Nat Med* 12(7) (2006) 809-16.
- [12] P. Vaupel, G. Multhoff, Fatal Alliance of Hypoxia-/HIF-1 $\alpha$ -Driven Microenvironmental Traits Promoting Cancer Progression, *Adv Exp Med Biol* 1232 (2020) 169-176.
- [13] X. Wang, L. Li, K. Zhao, Q. Lin, H. Li, X. Xue, W. Ge, H. He, D. Liu, H. Xie, Q. Wu, Y. Hu, A novel LncRNA HITT forms a regulatory loop with HIF-1 $\alpha$  to modulate angiogenesis and tumor growth, *Cell Death Differ* 27(4) (2020) 1431-1446.
- [14] J.M. Henk, P.B. Kunkler, C.W. Smith, Radiotherapy and Hyperbaric-Oxygen in Head and Neck Cancer - Final Report of 1st Controlled Clinical-Trial, *Lancet* 2(8029) (1977) 101-103.
- [15] P. Ma, H. Xiao, C. Yu, J. Liu, Z. Cheng, H. Song, X. Zhang, C. Li, J. Wang, Z. Gu, J. Lin, Enhanced Cisplatin Chemotherapy by Iron Oxide Nanocarrier-Mediated Generation of Highly Toxic Reactive Oxygen Species, *Nano Lett* 17(2) (2017) 928-937.
- [16] A.E. Nejad, S. Najafgholian, A. Rostami, A. Sistani, S. Shojaeifar, M. Esparvarinha, R. Nedaeinia, S.H. Javanmard, M. Taherian, M. Ahmadlou, R. Salehi, B. Sadeghi, M. Manian, The role of hypoxia in the tumor microenvironment and development of cancer stem cell: a novel approach to developing treatment, *Cancer Cell International* 21(1) (2021).
- [17] W. Tang, Z. Yang, L. He, L. Deng, P. Fathi, S. Zhu, L. Li, B. Shen, Z. Wang, O. Jacobson, J. Song, J. Zou, P. Hu, M. Wang, J. Mu, Y. Cheng, Y. Ma, L. Tang, W. Fan, X. Chen, A hybrid semiconducting organosilica-based O<sub>2</sub> nanoeconomizer for on-demand synergistic photothermally boosted radiotherapy, *Nat Commun* 12(1) (2021) 523.
- [18] X. Wang, Y. Mao, C. Sun, Q. Zhao, Y. Gao, S. Wang, A versatile gas-generator promoting drug release and oxygen replenishment for amplifying photodynamic-chemotherapy synergetic anti-tumor effects, *Biomaterials* 276 (2021) 120985.
- [19] X. Liu, N. Ye, S. Liu, J. Guan, Q. Deng, Z. Zhang, C. Xiao, Z.Y. Ding, B.X. Zhang, X.P. Chen, Z. Li, X. Yang, Hyperbaric Oxygen Boosts PD-1 Antibody Delivery and T Cell Infiltration for Augmented Immune Responses Against Solid Tumors, *Adv Sci (Weinh)* 8(15) (2021) e2100233.
- [20] L. You, W. Wu, X. Wang, L. Fang, V. Adam, E. Nepovimova, Q. Wu, K. Kuca, The role of hypoxia-inducible factor 1 in tumor immune evasion, *Med Res Rev* 41(3) (2021) 1622-1643.
- [21] J.D. Gordan, C.B. Thompson, M.C. Simon, HIF and c-Myc: sibling rivals for control of cancer cell metabolism and proliferation, *Cancer Cell* 12(2) (2007) 108-113.
- [22] B.R. Wilde, D.E. Ayer, Interactions between Myc and MondoA transcription factors in metabolism and tumorigenesis, *Br J Cancer* 113(11) (2015) 1529-33.
- [23] M.S. Nakazawa, B. Keith, M.C. Simon, Oxygen availability and metabolic adaptations, *Nat Rev Cancer* 16(10) (2016) 663-73.
- [24] S.M. Hatfield, J. Kjaergaard, D. Lukashev, T.H. Schreiber, B. Belikoff, R. Abbott, S. Sethumadhavan, P. Philbrook, K. Ko, R. Cannici, M. Thayer, S. Rodig, J.L. Kutok, E.K. Jackson, B. Karger, E.R. Podack, A. Ohta, M.V. Sitkovsky, Immunological mechanisms of the antitumor effects of supplemental oxygenation, *Sci Transl Med* 7(277) (2015) 277ra30.

- [25] Z. Jiu, Q. Zhao, S. Tian, W. Jiang, T. Hu, Strategies of Alleviating Tumor Hypoxia and Enhancing Tumor Therapeutic Effect by Macromolecular Nanomaterials, *Macromol Biosci* (2021) e2100092.
- [26] X. Liang, M. Chen, P. Bhattarai, S. Hameed, Z. Dai, Perfluorocarbon@Porphyrin Nanoparticles for Tumor Hypoxia Relief to Enhance Photodynamic Therapy against Liver Metastasis of Colon Cancer, *ACS Nano* 14(10) (2020) 13569-13583.
- [27] I. Godet, Y.J. Shin, J.A. Ju, I.C. Ye, G. Wang, D.M. Gilkes, Fate-mapping post-hypoxic tumor cells reveals a ROS-resistant phenotype that promotes metastasis, *Nat Commun* 10(1) (2019) 4862.
- [28] O. Thews, A. Riemann, Tumor pH and metastasis: a malignant process beyond hypoxia, *Cancer Metastasis Rev* 38(1-2) (2019) 113-129.
- [29] J.R. Wu, R.I. You, C.T. Hu, C.C. Cheng, R. Rudy, W.S. Wu, Hydrogen peroxide inducible clone-5 sustains NADPH oxidase-dependent reactive oxygen species-c-jun N-terminal kinase signaling in hepatocellular carcinoma, *Oncogenesis* 8(8) (2019) 40.
- [30] Z. Yu, P. Zhou, W. Pan, N. Li, B. Tang, A biomimetic nanoreactor for synergistic chemiexcited photodynamic therapy and starvation therapy against tumor metastasis, *Nat Commun* 9(1) (2018) 5044.
- [31] S.Y. Li, H. Cheng, B.R. Xie, W.X. Qiu, J.Y. Zeng, C.X. Li, S.S. Wan, L. Zhang, W.L. Liu, X.Z. Zhang, Cancer Cell Membrane Camouflaged Cascade Bioreactor for Cancer Targeted Starvation and Photodynamic Therapy, *ACS Nano* 11(7) (2017) 7006-7018.
- [32] C. Liu, J. Xing, O.U. Akakuru, L. Luo, S. Sun, R. Zou, Z. Yu, Q. Fang, A. Wu, Nanozymes-Engineered Metal-Organic Frameworks for Catalytic Cascades-Enhanced Synergistic Cancer Therapy, *Nano Lett* 19(8) (2019) 5674-5682.
- [33] D. Wang, H. Wu, W.Q. Lim, S.Z.F. Phua, P. Xu, Q. Chen, Z. Guo, Y. Zhao, A Mesoporous Nanoenzyme Derived from Metal-Organic Frameworks with Endogenous Oxygen Generation to Alleviate Tumor Hypoxia for Significantly Enhanced Photodynamic Therapy, *Adv Mater* 31(27) (2019) e1901893.
- [34] Q. You, K. Zhang, J. Liu, C. Liu, H. Wang, M. Wang, S. Ye, H. Gao, L. Lv, C. Wang, L. Zhu, Y. Yang, Persistent Regulation of Tumor Hypoxia Microenvironment via a Bioinspired Pt-Based Oxygen Nanogenerator for Multimodal Imaging-Guided Synergistic Phototherapy, *Adv Sci (Weinh)* 7(17) (2020) 1903341.
- [35] S.L. Li, P. Jiang, F.L. Jiang, Y. Liu, Recent Advances in Nanomaterial-Based Nanoplatforams for Chemodynamic Cancer Therapy, *Adv Funct Mater* 31(22) (2021).
- [36] Z.F. Ma, X.D. Jia, J. Bai, Y.D. Ruan, C. Wang, J.M. Li, M.C. Zhang, X. Jiang, MnO<sub>2</sub> Gatekeeper: An Intelligent and O<sub>2</sub>-Evolving Shell for Preventing Premature Release of High Cargo Payload Core, Overcoming Tumor Hypoxia, and Acidic H<sub>2</sub>O<sub>2</sub>-Sensitive MRI, *Adv Funct Mater* 27(4) (2017).
- [37] X. Mei, T. Hu, H. Wang, R. Liang, W. Bu, M. Wei, Highly dispersed nano-enzyme triggered intracellular catalytic reaction toward cancer specific therapy, *Biomaterials* 258 (2020) 120257.
- [38] X. Yang, Y. Yang, F. Gao, J.J. Wei, C.G. Qian, M.J. Sun, Biomimetic Hybrid Nanozymes with Self-Supplied H<sup>+</sup> and Accelerated O<sub>2</sub> Generation for Enhanced Starvation and Photodynamic Therapy against Hypoxic Tumors, *Nano Lett* 19(7) (2019) 4334-4342.
- [39] P. Yuan, G.L. Fan, L.P. Zhao, L.S. Liu, F.A. Deng, X.Y. Jiang, A.H. Hu, X.Y. Yu, A.L. Chen, H. Cheng, S.Y. Li, Tumor targeted self-synergistic nanoplatforams for arsenic-sensitized photodynamic therapy, *Acta Biomater* 117 (2020) 349-360.
- [40] Y. Chao, L. Xu, C. Liang, L. Feng, J. Xu, Z. Dong, L. Tian, X. Yi, K. Yang, Z. Liu, Combined local immunostimulatory radioisotope therapy and systemic immune checkpoint blockade imparts potent antitumour responses, *Nat Biomed Eng* 2(8) (2018) 611-621.
- [41] P. Pei, T. Liu, W.H. Shen, Z. Liu, K. Yang, Biomaterial-mediated internal radioisotope therapy, *Mater Horiz* 8(5) (2021) 1348-1366.
- [42] D. Feng, W.C. Chung, Z. Wei, Z.Y. Gu, H.L. Jiang, Y.P. Chen, D.J. Darensbourg, H.C. Zhou, Construction of ultrastable porphyrin Zr metal-organic frameworks through linker elimination, *J Am Chem Soc* 135(45) (2013) 17105-10.
- [43] C.H. Chang, J. Qiu, D. O'Sullivan, M.D. Buck, T. Noguchi, J.D. Curtis, Q.Y. Chen, M. Gindin, M.M. Gubin, G.J.W. van der Windt, E. Tonc, R.D. Schreiber, E.J. Pearce, E.L. Pearce, Metabolic Competition in the Tumor Microenvironment Is a Driver of Cancer Progression, *Cell* 162(6) (2015) 1229-1241.
- [44] J.E. Bader, K. Voss, J.C. Rathmell, Targeting Metabolism to Improve the Tumor Microenvironment for Cancer Immunotherapy, *Mol Cell* 78(6) (2020) 1019-1033.
- [45] F. Zheng, J. Chen, X. Zhang, Z. Wang, J. Chen, X. Lin, H. Huang, W. Fu, J. Liang, W. Wu, B. Li, H. Yao, H. Hu, E. Song, The HIF-1 $\alpha$  antisense long non-coding RNA drives a positive feedback loop of HIF-1 $\alpha$  mediated transactivation and glycolysis, *Nat Commun* 12(1) (2021) 1341.

- [46] Z. Chen, D. Han, X. Liao, T. Zhang, J. Xiao, W. Chen, Q. Liu, T. Chen, D. Li, L. Zhu, S. Cai, Apigenin Combined With Gefitinib Blocks Autophagy Flux and Induces Apoptotic Cell Death Through Inhibition of HIF-1 $\alpha$ , c-Myc, p-EGFR, and Glucose Metabolism in EGFR L858R+T790M-Mutated H1975 Cells, *Front Pharmacol* 10 (2019) 260.
- [47] F.R. Dejure, M. Eilers, MYC and tumor metabolism: chicken and egg, *EMBO J* 36(23) (2017) 3409-3420.
- [48] A. Palazon, A.W. Goldrath, V. Nizet, R.S. Johnson, HIF transcription factors, inflammation, and immunity, *Immunity* 41(4) (2014) 518-28.
- [50] P. Pei, W.H. Shen, H.L. Zhou, Y.C. Sun, J. Zhong, T. Liu, K. Yang, Radionuclide labelled gold nanoclusters boost effective anti-tumor immunity for augmented radio-immunotherapy of cancer, *Nano Today* 38 (2021) 101144.





**Scheme 1.** Schematic diagram of radioactive nano-oxygen generator to enhance anti-tumor immunotherapy by regulating tumor microenvironment and metabolism.



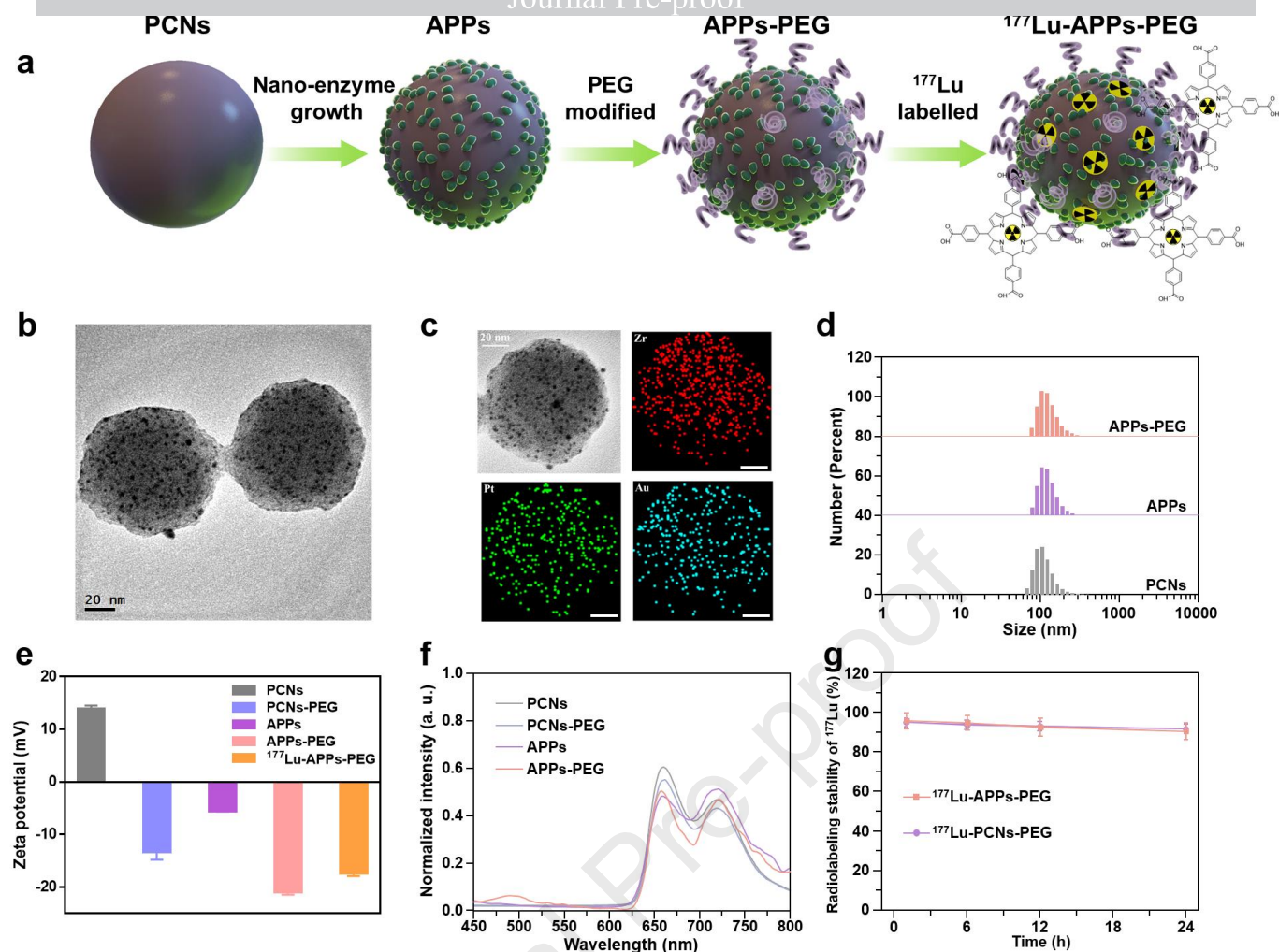


**Figure 1. The fabrication and characterization of radioactive nano-oxygen generator.** a) Synthetic procedure of radioactive nano-oxygen generator. b) TEM images of APPs. c) Elemental mapping images of APPs. d) DLS (dynamic light scattering) of PCNs, APPs and APPs-PEG. e) Zeta potential of PCNs, PCNs-PEG, APPs, APPs-PEG and  $^{177}\text{Lu}$ -APPs-PEG. f) Fluorescence spectra of PCNs, PCNs-PEG, APPs and APPs-PEG. g) Radio-labelling stability of  $^{177}\text{Lu}$ -PCNs-PEG and  $^{177}\text{Lu}$ -APPs-PEG.

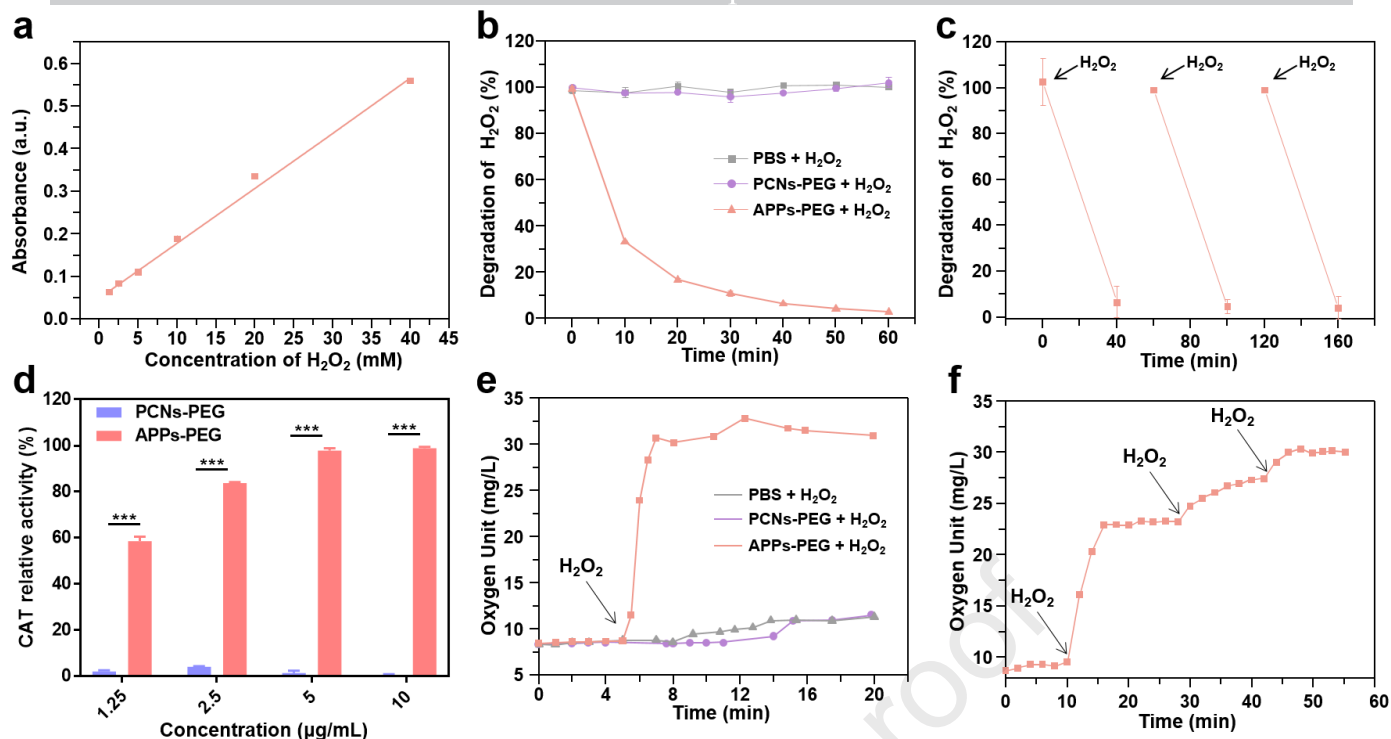


**Figure 2. Effectively decomposing hydrogen peroxide to produce oxygen.** **a)** UV-vis absorbance (405 nm) of  $\text{Ti}(\text{SO}_4)_2$  solution after treated with  $\text{H}_2\text{O}_2$  in different concentrations (1.25mM, 2.5mM, 5mM, 10mM, 20mM, 40mM). **b)**  $\text{H}_2\text{O}_2$  (10 mM) degradation after treated with PBS, PCNs-PEG and APPs-PEG (10  $\mu\text{g/mL}$ ) at different time points. **c)** Continuous  $\text{H}_2\text{O}_2$  consumption after treated with APPs-PEG by repetitive addition of  $\text{H}_2\text{O}_2$ . **d)** Catalase activity of APPs-PEG detected by CAT Kit at different concentrations. **e)** Curve of  $\text{O}_2$  generation after treated with PBS, PCNs-PEG and APPs-PEG at predesigned time points ( $\text{H}_2\text{O}_2$ : 10 mM, APPs-PEG: 10  $\mu\text{g/mL}$ ). **f)** Repetitive  $\text{O}_2$  generation after treated with APPs-PEG (10  $\mu\text{g/mL}$ ) by repeated addition of  $\text{H}_2\text{O}_2$ . P values in **d** were calculated by multiple t tests (\*\*\*P < 0.001, \*\*P < 0.01, \*P < 0.05).

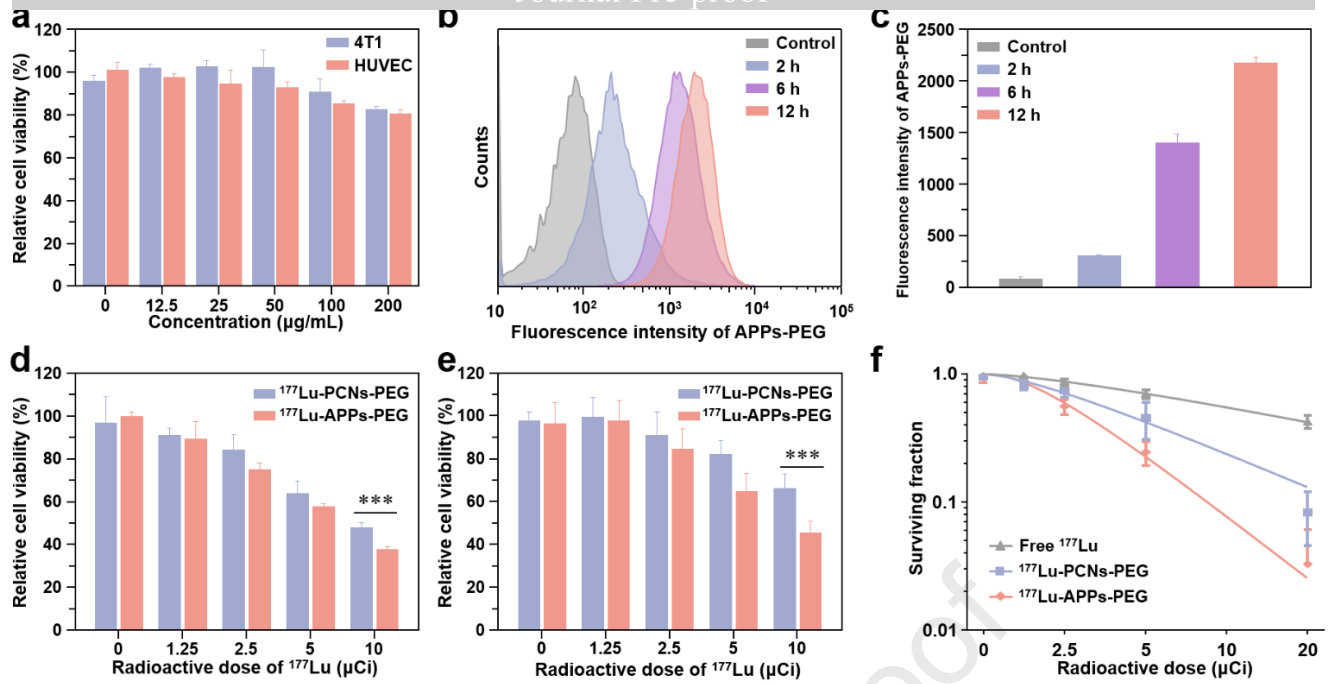


**Figure 3. In vitro evaluation of radioactive nano-oxygen generator.** **a)** Cytotoxicity of APPs-PEG at different concentrations. **b)** Flow cytometric analysis of 4T1 cells incubated with APPs-PEG. **c)** Statistic data of (b). Error bars represent mean  $\pm$  s.d. (n = 3). **d&e)** Cytotoxicity of different formulations ( $^{177}\text{Lu}$ -PCNs-PEG,  $^{177}\text{Lu}$ -APPs-PEG) incubated with 4T1 cells under normoxia (d) and hypoxia (e) conditions. **f)** Colongenic assay of 4T1 cells treated by  $^{177}\text{Lu}$ -APPs-PEG at different doses. P values in **d&e** were calculated by multiple t tests (\*\* $P < 0.001$ , \* $P < 0.01$ ,  $P < 0.05$ ).

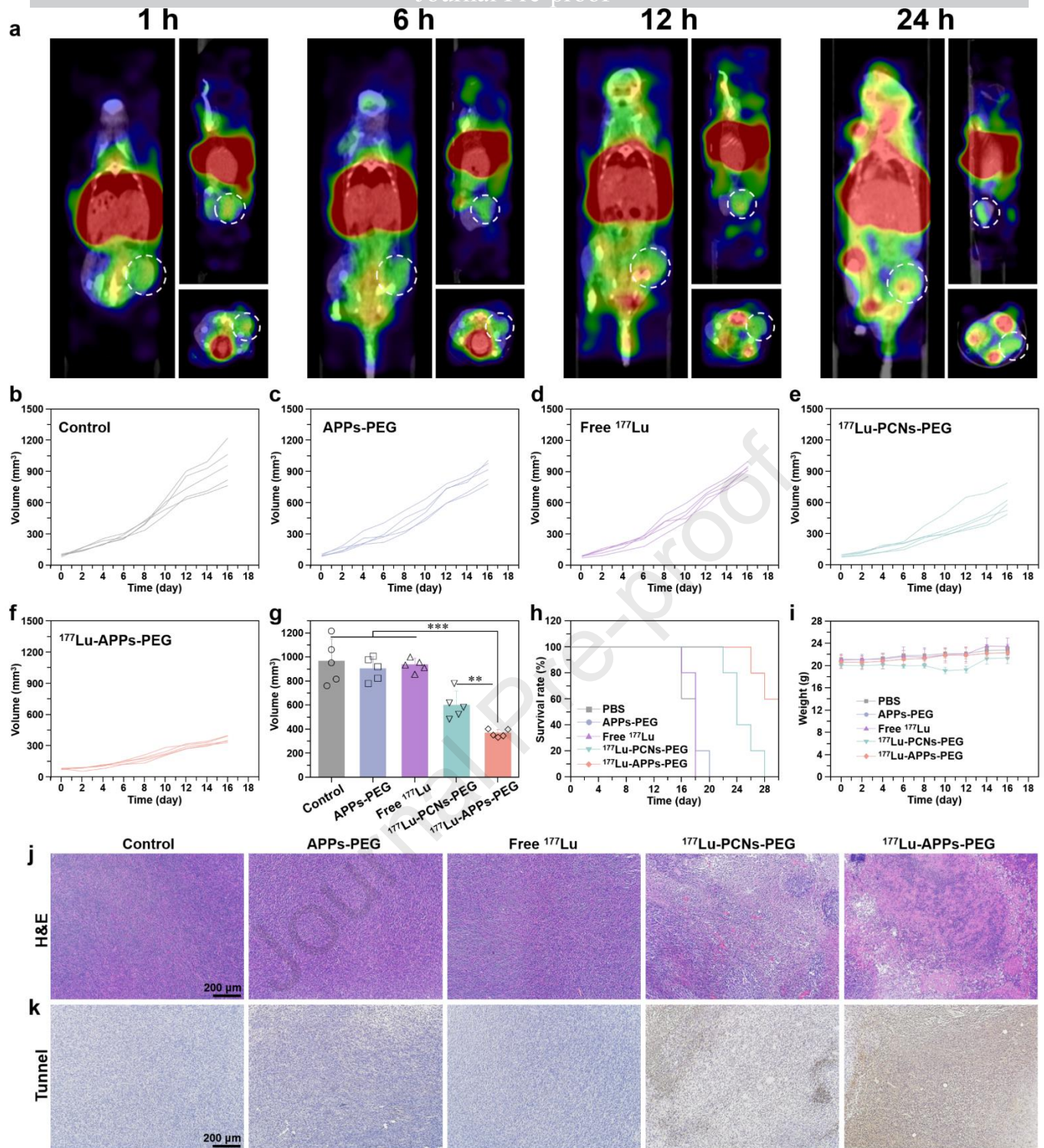


**Figure 4. Unfreezing the limitation of oxygen dependence of internal radioisotope therapy.** **a)** SPECT/CT images of 4T1 tumor-bearing mice post i.v. injected with  $^{177}\text{Lu}$ -APPs-PEG at different times. **b-f)** 4T1 tumor growth curves post treatments (Control (b), APPs-PEG (c), Free  $^{177}\text{Lu}$  (d),  $^{177}\text{Lu}$ -PCNs-PEG (e), ( $^{177}\text{Lu}$ -APPs-PEG (f)). **g)** Statistics and analysis of tumor volume at 16 day post treatments. **h)** Survivorship curves of mice post treatments. **i)** Body weight changes of mice post treatments. **j&k)** Micrographs of H&E (j) and TUNEL (k) stained tumor slices from mice collected 3 days after treatment. P values in **g** were calculated by multiple t tests (\*\*\*P < 0.001, \*\*P < 0.01, \*P < 0.05).



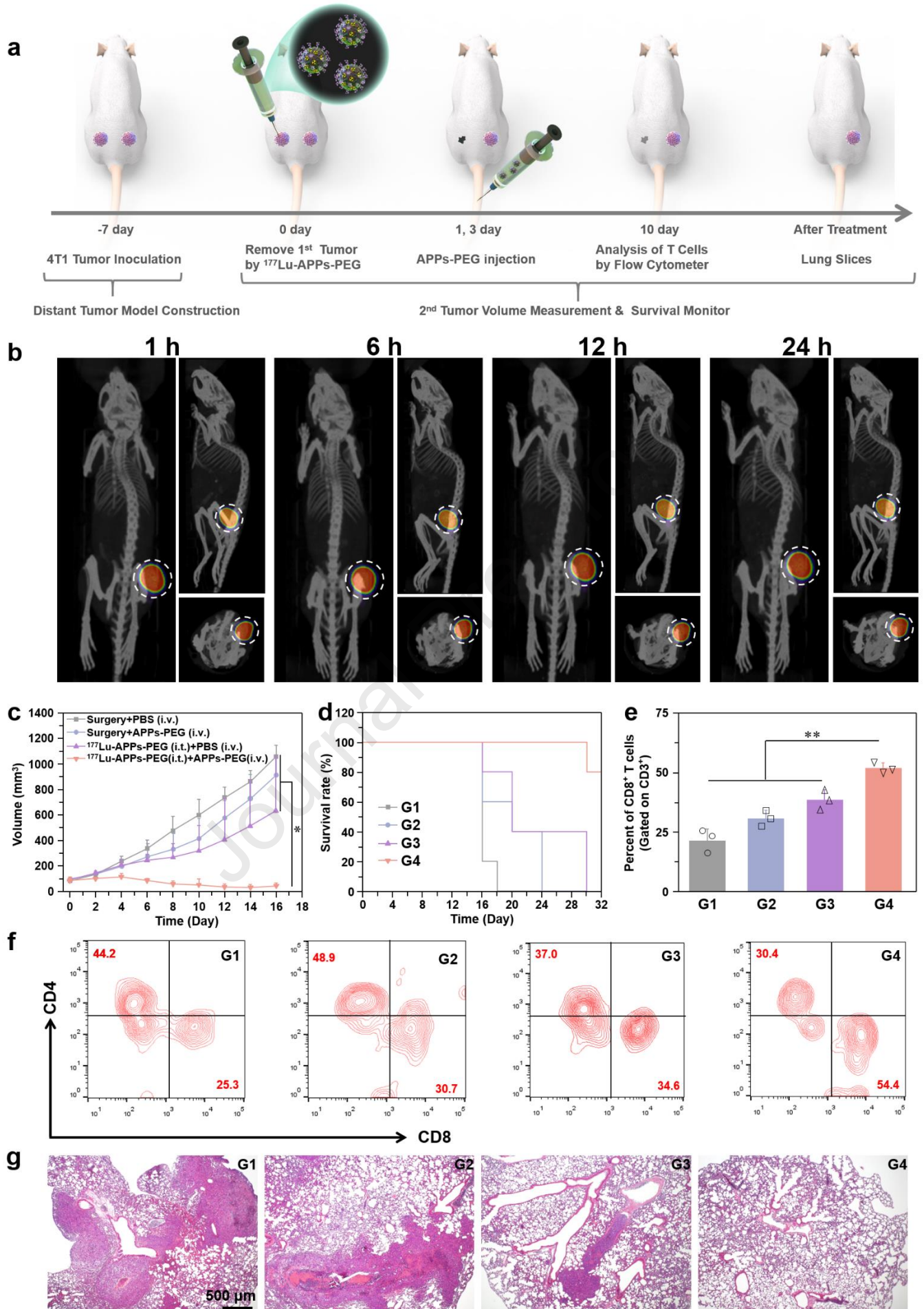


**Figure 5. Boosting antitumor immune response to distal tumors by nano-oxygen generator.** a) Schematic diagram of local RIT plus APPs-PEG to suppress the growth of distal tumors. b) SPECT/CT images of 4T1 tumor-bearing mice post i.t.

injection of  $^{177}\text{Lu}$ -APPS-PEG at different time points. **c)** Distant tumour growth curves and **d)** survival curves of mice after post treatments ( $n = 5$ ). **e)** Proportions of tumor-infiltrating CD8<sup>+</sup> killer T cells among CD3<sup>+</sup> cells and **f)** representative flow cytometry plots showing different types of T cells in the secondary tumors from different groups 7 days post treatment. Error bars represent mean  $\pm$  s.d. ( $n = 3$ ). **g)** H&E slices of lung collected from mice at 25 day after treatments. (G1: Surgery + PBS (i.v.), G2: Surgery + APPs-PEG (i.v.), G3:  $^{177}\text{Lu}$ -APPS-PEG (i.t.) + PBS (i.v.), G4:  $^{177}\text{Lu}$ -APPS-PEG (i.t.) + APPs-PEG (i.v.)). P values in **c** and **e** were calculated by multiple t tests (\*\*\*P < 0.001, \*\*P < 0.01, \*P < 0.05)



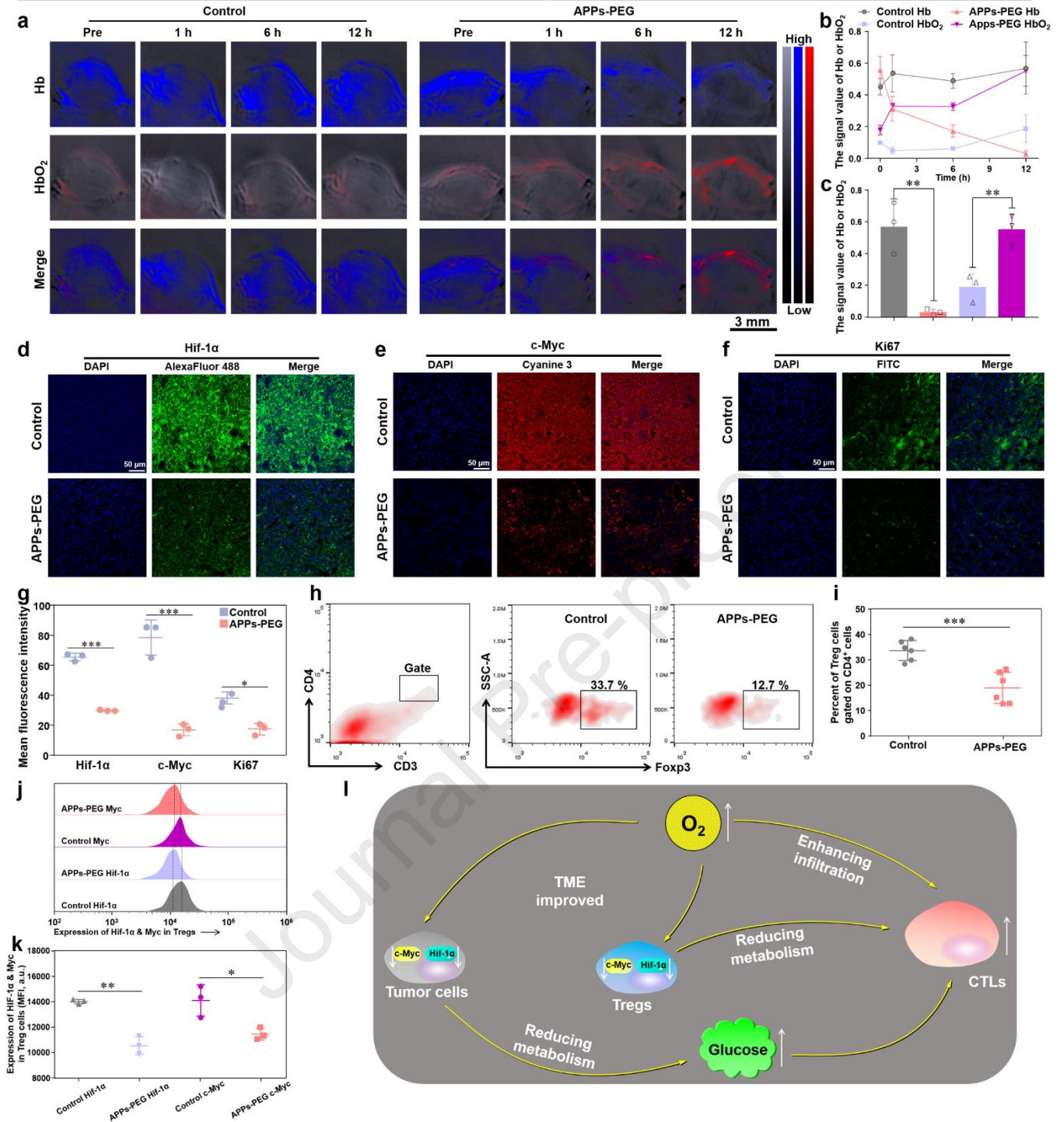


**Figure 6. Slowing down the proliferation of Treg cell and tumor cell by regulating TME and glycometabolism.** **a)** Photoacoustic imaging showing tumors deoxyhemoglobin (Hb) and oxyhemoglobin (HbO<sub>2</sub>) after i.v. injection of APPs-PEG and PBS at different time points. **b)** The signal value of tumor Hb and HbO<sub>2</sub> at different time points. Error bars represent mean ± s.d. (n = 3). **c)** Statistic data of (b) at 12 h. **d)** The immunofluorescence slices of HIF-1α expression in tumors (blue: nucleus, green: HIF-1α). **e)** The immunofluorescence slices of c-Myc expression in tumors (blue: nucleus, red: c-Myc). **f)** The immunofluorescence slices of Ki67 expression in tumors (blue: nucleus, green: Ki67). **g)** Fluorescence intensity statistics of d, e and f, which were calculated by Image J. Error bars represent mean ± s.d. (n = 3). **h)** Representative flow cytometry plots of CD3+CD4+FoxP3+ regulatory T (Treg) cells in 4T1 tumors 4 days post treatment. **i)** Proportions of CD3+CD4+FoxP3+ regulatory T cells among CD4+ cells. Error bars represent mean ± s.d. (n = 6). **j)** and **k)** Representative histograms (j) and statistic data (k) of HIF-1α and c-Myc expression in Treg cells from tumors. Error bars represent mean ± s.d. (n = 3). **l)** Mechanistic diagram of the role of O<sub>2</sub> produced by nano-oxygen generator in anti-tumor immune response and TME metabolism. P values in c, g, i and k were calculated by multiple t tests (\*\*P < 0.01, \*\*\*P < 0.001, \*P < 0.05).

**Declaration of interests**

☒ The authors declare that they have no known competing financial interests or personal relationships that could have appeared to influence the work reported in this paper.

☐ The authors declare the following financial interests/personal relationships which may be considered as potential competing interests:

--